Supporting information

Seawater Battery Performance Enhancement Enabled by Defect/Edge-rich, Oxygen Self-doped Porous Carbon Electrocatalyst

S. T. Senthilkumar[a], Sung O Park[a], Junsoo Kim[a], Soo Min Hwang[a], Sang Kyu Kwak[a,*] and Youngsik Kim[a,b,*]

[a]*School of Energy & Chemical Engineering, Ulsan National Institute of Science and Technology (UNIST), Ulsan 689-798, Republic of Korea*
[b]*Energy Materials and Devices Lab, 4TOONE Corporation, UNIST-gil 50, Ulsan 689-798, Republic of Korea*
E-mail: ykim@unist.ac.kr (Y. Kim); skkwak@unist.ac.kr (S.K.Kwak)

S1. Experimental

Preparation of porous carbon catalyst

To prepare the porous carbon, a bio-waste, *grapefruit (Citrus paradise) peel* was used as a precursor for carbon sources. First, the grapefruit peel was cut into small species and washed with distilled water. Then, the washed grapefruit peel waste was placed into a Teflon-lined stainless steel autoclave with 80 mL of distilled water and sealed, heated at 180 °C for 24 h, and allowed to cool to room temperature. The resulting sample was washed with distilled water and dried at 100 °C overnight. After that, the hydrothermally treated sample was activated with NaOH and carbonized in a tube furnace at 800 °C for 3 h under N_2 atmosphere. Afterward, the carbonized sample was thoroughly washed with the desired amount of HCl and distilled water. Then, the washed sample was dried at 80 °C overnight.

Characterizations of catalyst

Powder X-ray diffraction (XRD) patterns were collected (Rigaku D/MAX 2500V/PC) using an X-ray diffractometer equipped with a Cu Kα (at 40 KV and 200 mA) radiation over the 2θ range of 10-80°. The Raman spectra were obtained using a WITec alpha300R couple with a He-Ne laser of 532 nm at 1.0 mW. The morphologies of the samples were observed using scanning electron microscopy (SEM, Quanta 200, FEI). The microstructure of the catalyst was performed using a transmission electron microscope, HR-TEM (JEOL, JEM 2100F) with an accelerating voltage of 200 kV. Specific surface area was calculated from the results of N_2 physisorption at 77 K (Micromeritics ASAP 2020) by using the BET (Brunauer–Emmet–Teller) equation and pore size distributions of the sample were calculated using the BJH (Barrett–Joyner–Halenda) method. X-ray photoelectron spectroscopy (XPS) measurements were performed on ESCLAB 250Xi equipped with a monochromatic Al Kα X-ray source (1486.6 eV).

Evaluation of electrocatalytic OER/ORR activity

The OER/ORR activities were measured using a rotating disk electrode (RDE) and a three-electrode electrochemical cell. A Pt wire, Ag/AgCl, and glassy carbon rotating disk electrode were used as a counter, reference and working electrode. The electrolyte used in OER/ORR was natural seawater[1]. The catalyst inks in this work were prepared using the following formulation. 8 mg of catalyst (PC, 20% Pt/C, IrO, Vulcan X76 and re-heat-treated PC) was mixed in a glass vial with 0.25 ml of Nafion 5 wt% dispersion solution (Sigma-Aldrich), 0.75 ml of ethanol and 40µl of deionized water. The inks were sonicated for 1 h and then coated onto a glassy rotating disk electrode with a 3 mm diameter, and dried naturally. The working electrode was cycled at least 15 times before the data were recorded at a scan rate of 50 mV s^{-1}. To examine

OER activities in seawater, the LSV measurement was carried out at a scan rate of 10 mV s^{-1}. For CV measurement, a flow of O_2 was continued over the seawater during the CV recording to ensure its continuous O_2 saturation. Also, the CV was performed in N_2 saturated seawater by switching into N_2 flow. Before the RDE measurements, the electrolyte was saturated by bubbling O_2 or N_2 for 15 min. The RDE measurements were performed at different rotating rates varying from 400 to 1600 rpm with a scan rate of 10 mV s^{-1}. Koutecky-Levich (K-L) plots (J^{-1} vs. $\omega^{-1/2}$) were evaluated at various potentials. The slope of their best linear fit lines was used to calculate the number electrons transferred (n) on the basis of the following:

$$\frac{1}{J} = \frac{1}{J_L} + \frac{1}{J_K} = \frac{1}{B\omega^{1/2}} + \frac{1}{J_K} \qquad (1)$$

where, J is the measured disk current density; J_K and J_L are the kinetic and diffusion limiting current densities, respectively; and ω is the electrode rotation speed. B is the so-called "B-factor", which is given by the following equation,

$$B=0.2nFC_oD_o^{2/3}\nu^{-1/6} \qquad (2)$$

where n is the apparent number of electrons transferred in the reaction, F is the Faraday constant (96485 C mol^{-1}), D_o is the diffusion coefficient of O_2 in seawater (1.4×10^{-5} cm^2 s^{-1})[2], ν and C_o are the kinetic viscosity of the solution (0.1 $cm^2 s^{-1}$)[2] and the concentration of O_2 dissolved in seawater (0.25 mol cm^{-3})[2]. The constant 0.2 is adopted when the rotation speed is expressed in rpm.

Preparation of air cathode, anode, and solid electrolytes for seawater battery

The catalyst coated air-cathode electrode was prepared as follows. First, the catalyst paste was made by mixing of catalyst (80 wt%), SuperP (10 wt%) and poly (vinylidene) fluoride (10 wt%; PVDF) with N-methyl-2- pyrrolidone. Then, the paste was homogeneously coated on the one side of carbon felt (Fuel Cell Store, Inc.,) in the area of 2 cm^2. Finally, carbon felts were dried again at 80 °C in the oven and used as the air-cathode (air-electrode). The anode electrode for the half-cell was prepared by attaching a Na metal (Sigma-Aldrich) on the surface of the Ni mesh.

The anode electrode for the full cell is prepared as follows: First, a slurry was made by mixing of hard carbon (80 wt%), SuperP (10 wt%) and poly (vinylidene) fluoride (10 wt%; PVDF) with N-methyl-2-pyrrolidone. Then, the slurry was homogeneously coated on copper foil using the doctor-blade technique and dried at 80 °C in the oven.

NASICON was prepared by a solid-state reaction based on our previous report.[3–5] $Na_3PO_4 \cdot 12H_2O$, SiO_2 and ZrO_2 (from Aldrich, St Louis, MO, USA) were mixed and then calcined at 400 ° C and 1100 °C. After repeated mixing and calcination, the powder was pressed into a pellet, which was subsequently sintered at 1230 °C. The organic liquid electrolyte (1 M $NaCF_3SO_3$ in TEGDME) and seawater were purchased from Sigma-Aldrich.

Seawater battery assembly

Natural seawater was used as the cathode[1]. For the cathode current collector, a Ti mesh (Wooilmetal Corporation) and a sheet of carbon paper (Fuel Cell store) were used. A 0.8 mm-thick NASICON-type solid electrolyte ($Na_3Zr_2Si_2PO_{12}$) with a diameter of 16 mm was prepared according to previous works[3–5]. For the anode compartment, the solid electrolyte was mounted in the open-structured anode top holder and then sealed with the anode bottom holder, which contained an organic electrolyte of 1 M $NaCF_3SO_3$ (Sigma-Aldrich) in TEGDME (Sigma-Aldrich) and Ni tap (anodic current collector, Solbrain LTK) attached to Na metal or hard carbon electrode. The assembly process was carried out in a glove box under a high-purity Ar atmosphere (O_2 and H_2O less than 1 ppm). The assembled cells which consisted of Ni tap|anode|organic electrolyte|NASICON|saltwater|carbon paper|Ti mesh were immersed in seawater for electrochemical tests.

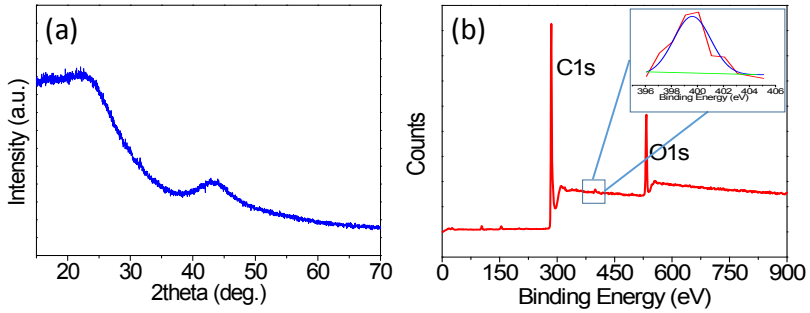

Fig. S1. (a) XRD pattern of the as-prepared porous carbon (PC) and (b) XPS survey spectra of the as-prepared PC and deconvoluted N 1s spectra (inset).

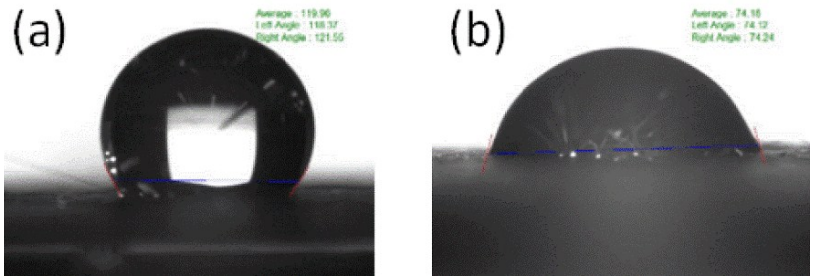

Fig. S2. Illustrating the changes of seawater contact angle of the carbon paper before and after coating the porous carbon catalysts. (a) Carbon paper and (b) porous carbon catalysts coated carbon paper.

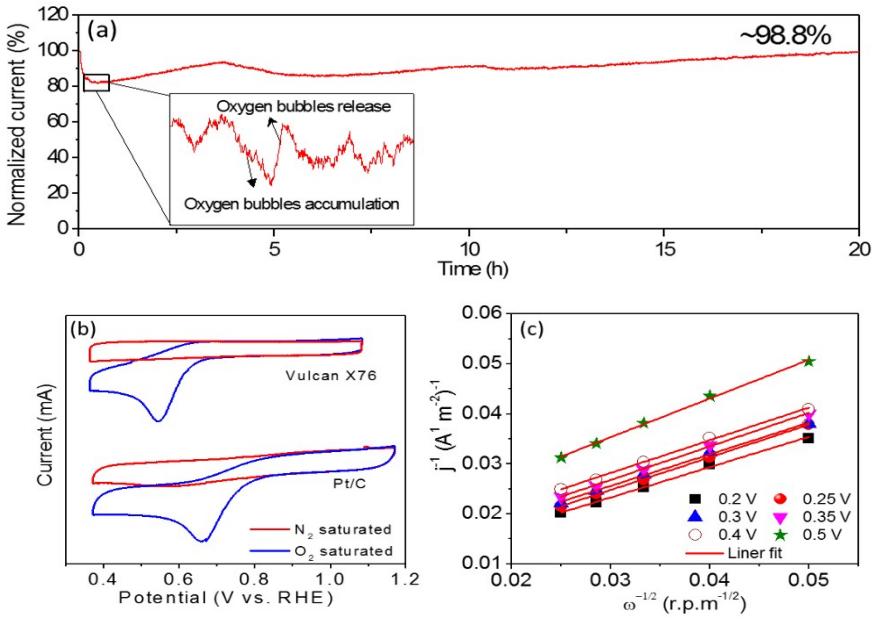

Fig. S3. Chronoamperometric test of porous carbon (PC) at 1.8 V vs. RHE, (b) Cyclic voltammetry curves (CV) of Pt/C and Vulcan X76 for ORR and (c) Koutechy-Levich (K-L) plots of the PC catalyst at different potentials.

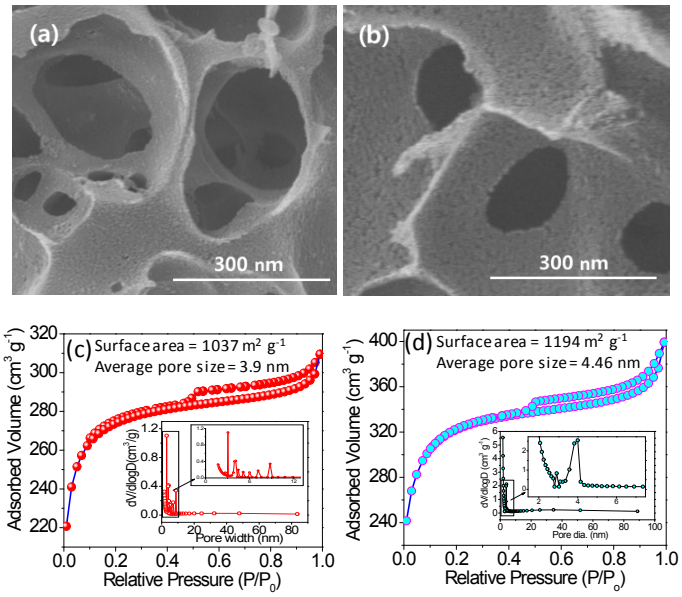

Fig. S4. SEM images of (a) as-prepared and (b) heat-treated (at 900 °C) PC powders and N_2 adsorption-desorption isotherm curve and pore size distribution (inset) of (c) the as-prepared PC and (d) heat-treated PC (at 900 °C).

We examine the pore morphology changes of heat treated PC using SEM. Fig. S4a and b shows the SEM image of the as-prepared PC and heat treated PC where it can be seen that the pore structure is stable, not collapsed after heat treatment. But, the walls of the pore have surface small pores after heat treatment (Fig. S4b) which could provide addition surface area. Then, we measured the BET surface area of the heat treated (at 900 °C) porous carbon and compared with as prepared PC. Fig. S4c and d shows the N_2 adsorption-desorption isotherm curve and pore size distribution (inset) of the as-prepared PC and heat treated PC. The BET results show that the surface area is slightly increased from 1037 m^2 g^{-1} to 1194 m^2 g^{-1} after heat treatment of PC (at 900 °C) which might be due to increasing degree of pores or pore size alteration. From the pore analysis (inset Fig. S4c) results it is found that after heat-treatment the peak intensity in the mesopores ranges increased, while the average pore size also increased from 3.9 nm to 4.46 nm.

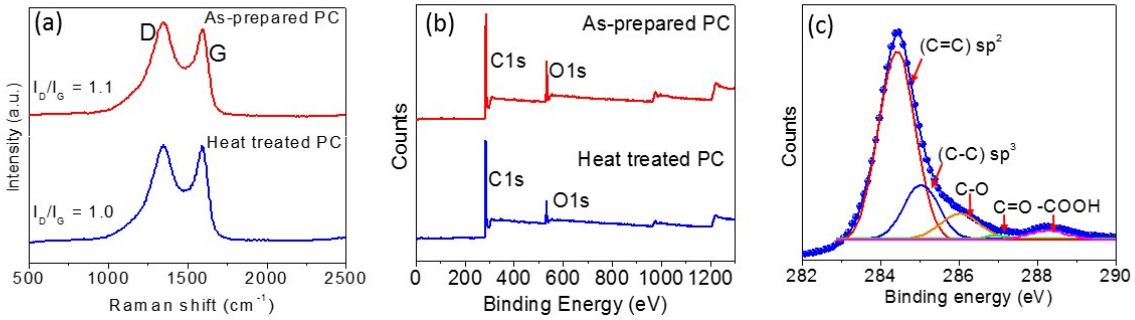

Fig. S5. (a) Raman spectra of the as-prepared porous carbon (PC) and heat treated PC, (b) XPS survey spectra of the as-prepared PC and heat treated PC and (c) C1s peak in the XPS spectrum of the heat treated carbon.

S2. Model system and theoretical methods

Density functional theory (DFT) was employed to investigate OER/ORR activities of porous carbon materials. We used Dmol[3] program to conduct the DFT calculation[6,7]. In order to describe exposed active sites for OER/ORR, we constructed functionalized one-dimensional (1D) zigzag and armchair graphene nanoribbons (GNRs) for edge sites and two-dimensional (2D) graphene for the sp^2-carbon atoms and sp^3-bonded defects. Based on the XPS results, functional groups were selected to be -COOH, -O, and =O (Fig. S6), where -O could be attributed to -OH or -O- functional groups. Note that 25% functionalized edges were considered in GNR models with H-termination. Also, layered graphenes were identified by HR-TEM image so that bilayer graphenes were considered to explain the effect of van der Waals interaction on catalytic activity. The generalized gradient approximation (GGA) with Perdew-Burke-Ernzerhof (PBE) functional[8] was employed with all electron core treatment including relativistic effect to optimize the model systems of our interest. Spin unrestricted calculation was performed with the basis set of DNP 4.4 level and DFT-D2(Grimme) method[9] was adopted for dispersion corrections. The effect of implicit water environment was applied by using the conductor-like screening model (COSMO),[10] where the dielectric constant of water was set to 78.54. Convergence tolerance of energy, maximum force, and maximum displacement during geometry optimization was set to 1.0×10^{-5} Ha, 0.002 Ha/Å, and 0.005 Å, respectively, in which self-consistent field tolerance criterion was less than 1.0×10^{-5} Ha. Zigzag GNR, armchair GNR, monolayer, and bilayer graphenes were constructed in a simulation with 20 Å vacuum regions, which were sampled with 1×2×1, 2×1×1, 2×2×1, and 2×2×1 Monkhorst-Pack *k*-point grids, respectively. Optimized systems of all intermediate steps were presented in Fig. S7-S9.

During the charging process, OER could occur in neutral solution by the reaction mechanisms as follows,

$$H_2O\,(l) + {}^* \rightarrow OH^* + H^+\,(aq) + e^- \qquad \backslash^* \text{ MERGEFORMAT (1)}$$

$$OH^* \rightarrow O^* + H^+\,(aq) + e^- \qquad \backslash^* \text{ MERGEFORMAT (2)}$$

$$H_2O\,(l) + O^* \rightarrow OOH^* + H^+\,(aq) + e^- \qquad \backslash^* \text{ MERGEFORMAT (3)}$$

$$OOH^* \rightarrow O_2\,(g) + H^+\,(aq) + e^- \qquad \backslash^* \text{ MERGEFORMAT (4)}$$

where * denotes the active site on the graphene, (*l*) and (*g*) indicate liquid and gas phases, respectively, and OH^*, O^*, OOH^* are adsorbate intermediates. During the discharging process, ORR could proceed through the simple four-electron pathway in neutral solution as follows,[4]

$$H_2O\,(l) + O_2\,(g) + {}^* + e^- \rightarrow OOH^* + OH^-\,(aq) \qquad \backslash^* \text{ MERGEFORMAT (5)}$$

$$OOH^* + e^- \rightarrow O^* + OH^-\,(aq) \qquad \backslash^* \text{ MERGEFORMAT (6)}$$

$$H_2O\,(l) + O^* + e^- \rightarrow OH^* + OH^-\,(aq) \qquad \backslash^* \text{ MERGEFORMAT (7)}$$

$$OH^* + e^- \rightarrow {}^* + OH^-\,(aq) \qquad \backslash^* \text{ MERGEFORMAT (8)}$$

Then, the change of Gibbs free energy for each reaction step was calculated by the following equation,[11,12]

$$\Delta G = \Delta E_{rxn} + \Delta E_{ZPE} - T\Delta S + \Delta G_U + \Delta G_{pH} \qquad \backslash^* \text{ MERGEFORMAT (9)}$$

where ΔE_{rxn} is the heat of reaction, ΔE_{ZPE} and ΔS represent the change of zero-point energy and entropy, respectively, which were obtained from vibrational calculations, T is temperature (i.e. 298K), and ΔG_U and ΔG_{pH}, which represent the contributions of electrode potential and proton concentration on the free energy, respectively, which were calculated by $\Delta G_U = -e\mathrm{U}$ and $\Delta G_{pH} = -\mathrm{pH} \times k_B T \ln 10$. Note U is the electrode potential (*vs.* standard hydrogen electrode) and k_B is the Boltzmann constant.

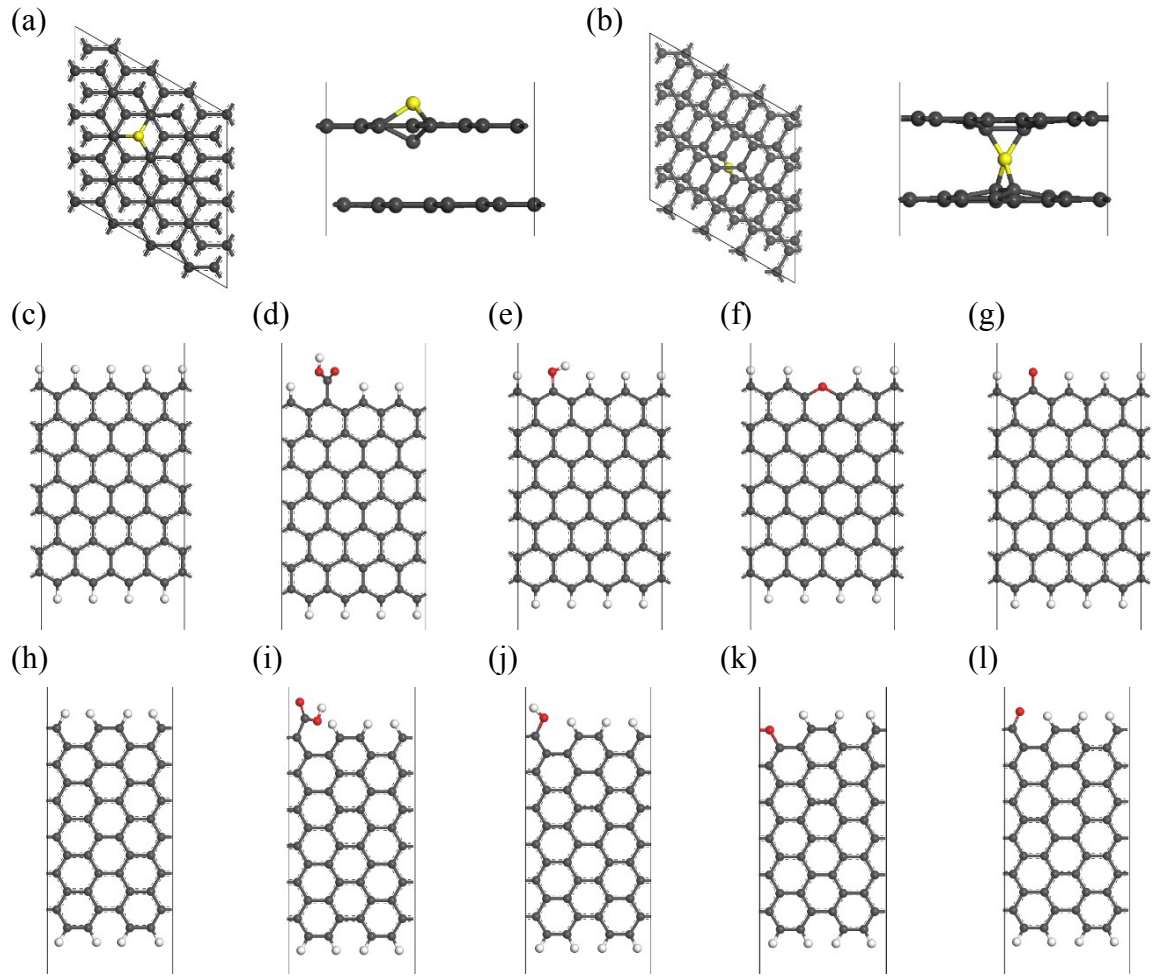

Fig. S6. Optimized systems of sp^3-type 1 defect, which could be induced by an interstitial carbon atom (yellow sphere) on graphene surface for (a) top and side views, and that of sp^3-type 2 defect, which is located in the middle of graphene sheets for (b) top and side views. For edge models, zigzag GNR (c) ~ (g) for fully H-terminated, -COOH, -OH, -O-, and =O functionalized models, respectively. Armchair GNR (h) ~ (l) for fully H-terminated, -COOH, -OH, -O-, and =O functionalized models, respectively. Dark gray, red, and white spheres represent carbon, oxygen, and hydrogen atoms, respectively.

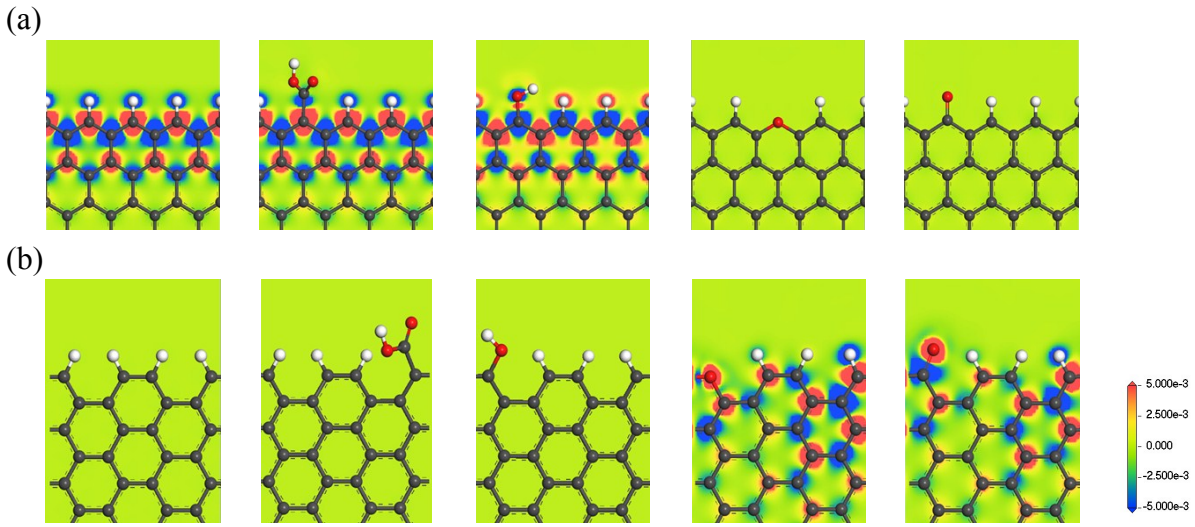

Fig. S7, Spin densities of fully H-terminated, -COOH, -OH, -O-, and =O functionalized (a) zigzag and (b) armchair GNRs. Dark gray, red, and white spheres represent carbon, oxygen, and hydrogen atoms, respectively.

Table S1. Overpotentials of our model systems for OER and ORR. The theoretical overpotential of IrO_2 was from reference[13].

		OER (eV)	ORR (eV)
Monolayer G		1.36	2.05
Bilayer G		1.29	1.94
sp^3-type 2		0.98	1.40
sp^3-type 1		0.65	0.85
Zigzag GNR	H-terminated	0.76	0.49
	-COOH	0.73	0.44
	-OH	0.79	0.55
	-O-	0.90	1.15
	=O	1.99	2.04
Armchair GNR	H-terminated	1.07	1.70
	-COOH	1.09	1.37
	-OH	1.85	1.65
	-O-	0.54	1.29
	=O	0.76	0.73
IrO_2		0.56[9]	-

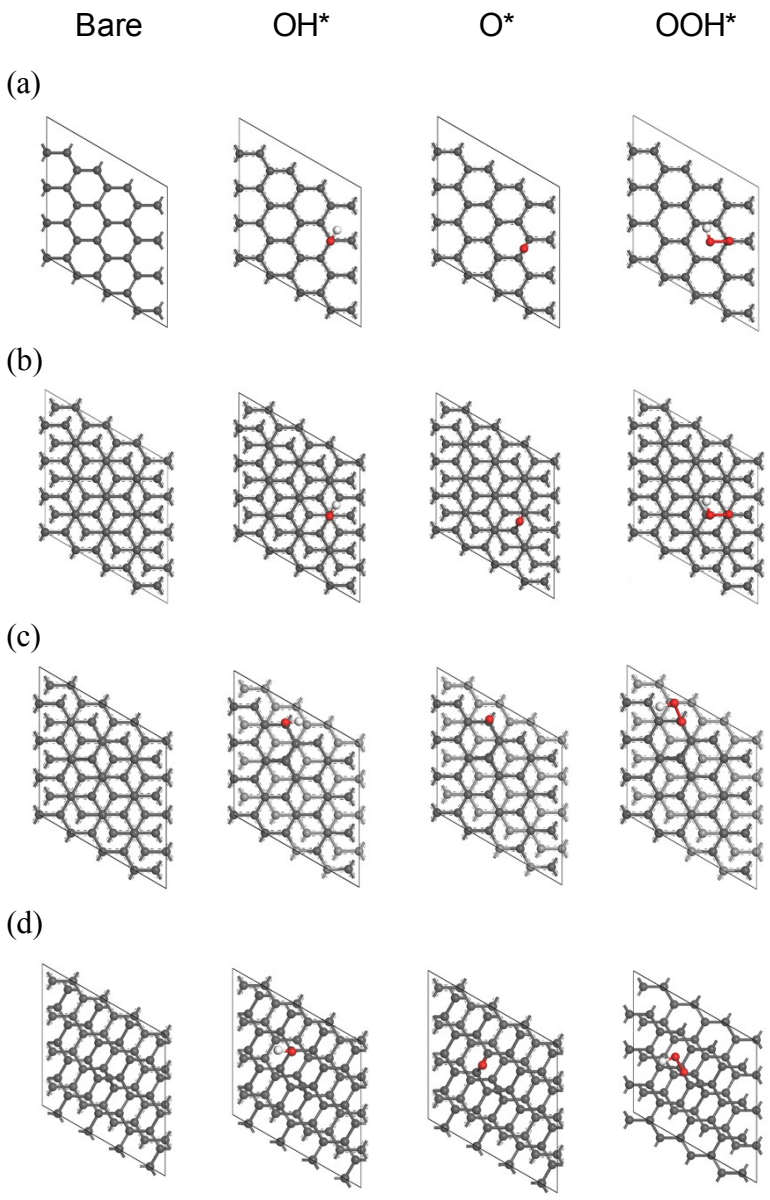

Fig. S8. Optimized systems of the intermediate states on (a) monolayer, (b) bilayer graphene, (c) sp^3-type 1 defect and (d) sp^3-type 2 defect. Dark gray, red, and white spheres represent carbon, oxygen, and hydrogen atoms, respectively.

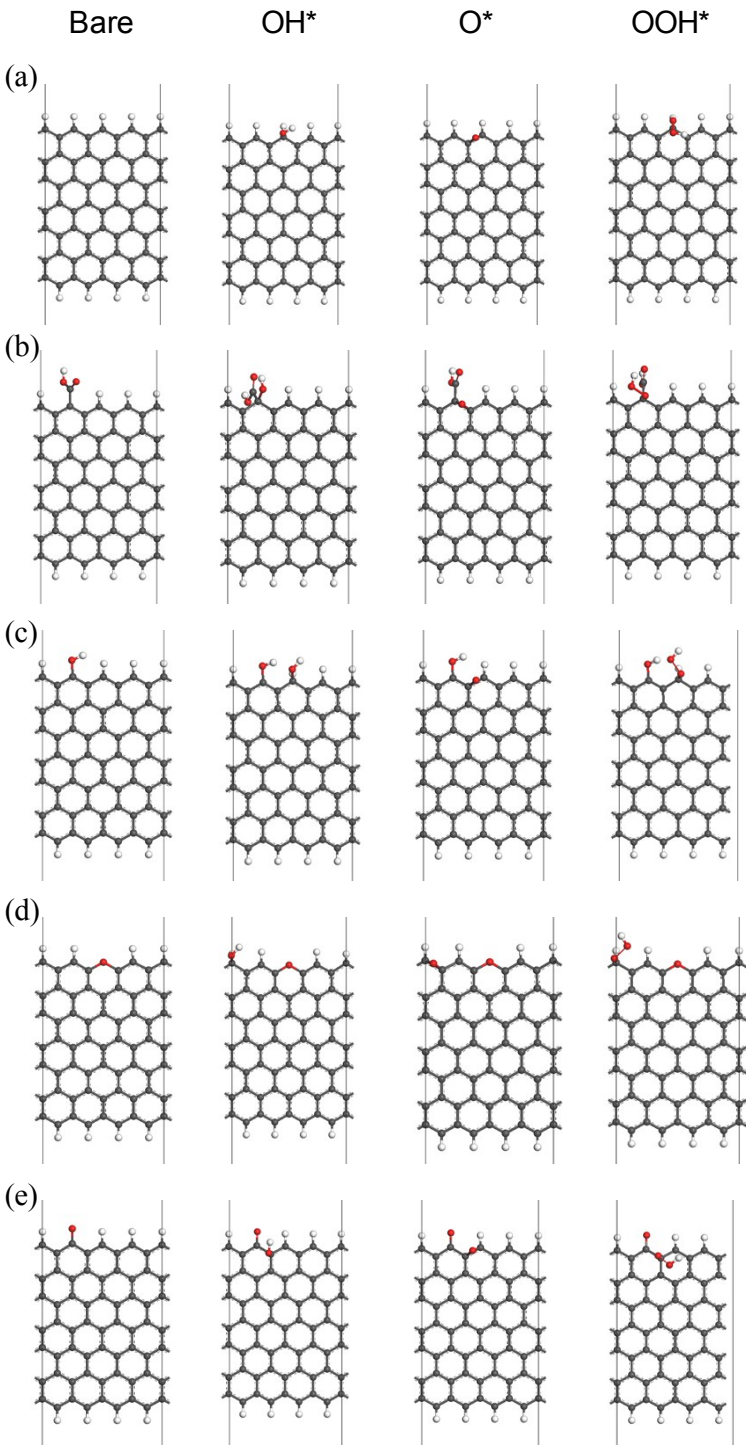

Fig. S9. Optimized systems of the intermediate states on (a) fully H-terminated, (b) -COOH, (c) -OH, (d) -O-, and (e) =O functionalized zigzag GNR. Dark gray, red, and white spheres represent carbon, oxygen, and hydrogen atoms, respectively.

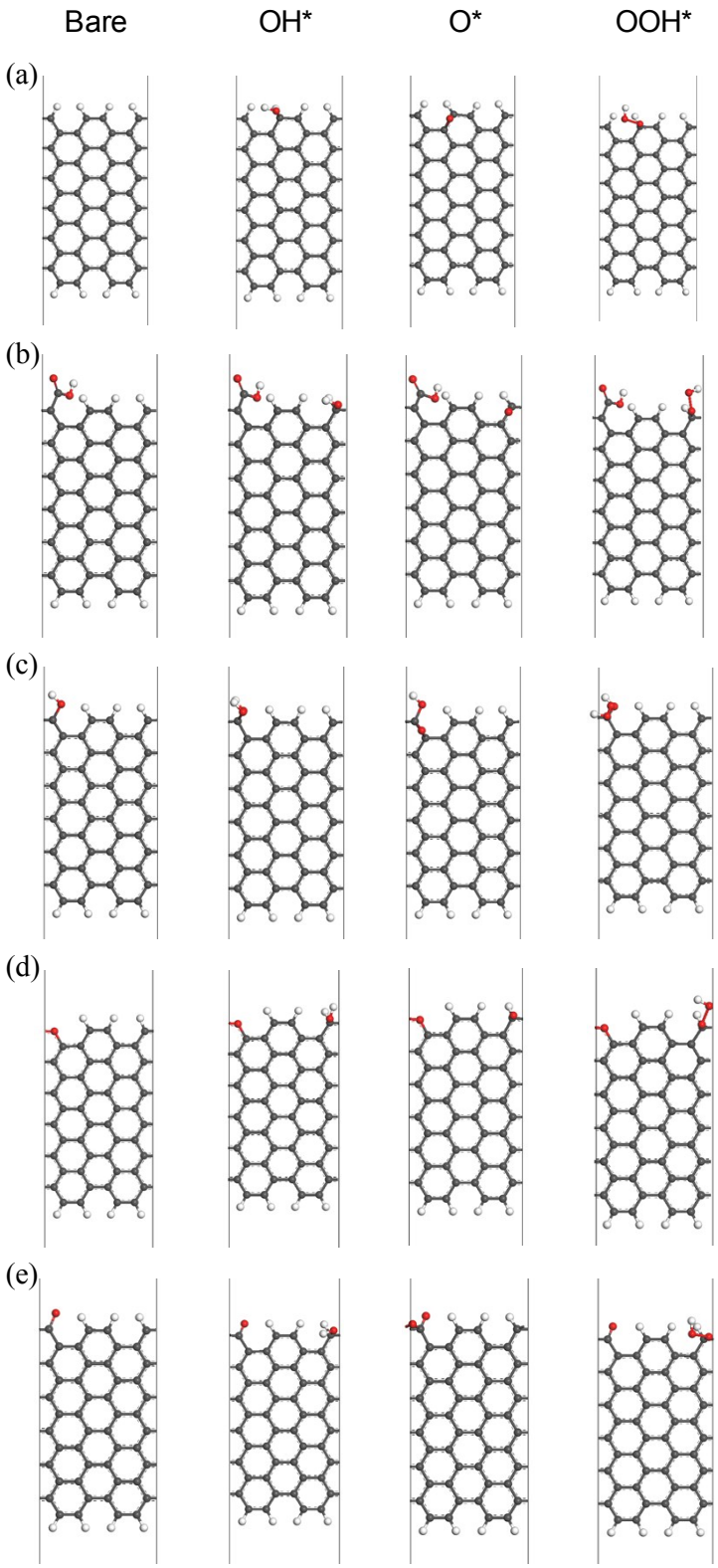

Fig. S10. Optimized systems of the intermediate states on (a) fully H-terminated, (b) -COOH, (c) -OH, (d) -O-, and (e) =O functionalized armchair GNR. Dark gray, red, and white spheres represent carbon, oxygen, and hydrogen atoms, respectively.

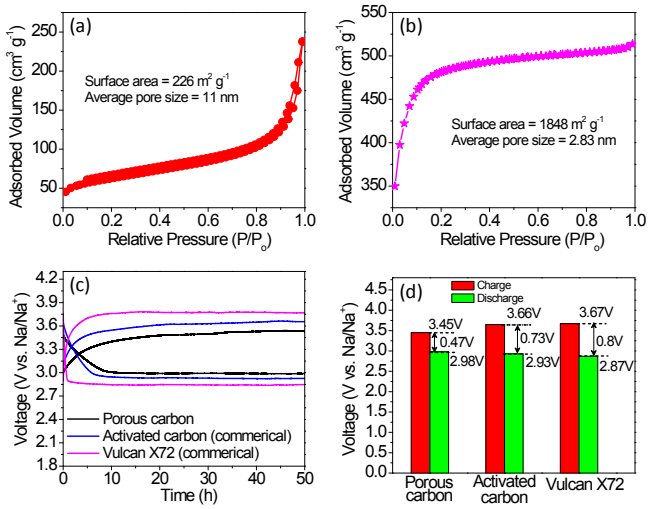

Fig. S11. N_2 adsorption-desorption isotherm curve of (a) Vulcan X72 and (b) activated carbon (commercial), (c) Charge-discharge curve of cathode half cell (Na|seawater|PC@carbon paper) with PC@carbon paper for 50 h at 0.01 mA cm^{-2} and compared with Vulcan X72 and activated carbon (commercial) and (d) Comparison of potential differences of PC, Vulcan X72 and activated carbon (commercial).

Table S2. Comparison of surface area and voltage gap of PC, Vulcan X72 and activated carbon (commercial).

Sample	Surface area (m^2 g^{-1})	Voltage gap (ΔV)	Current density (mA cm^{-2})
PC	1037	~0.47	0.01
Activated carbon (AC)	1848	~0.73	0.01
Vulcan X72	226	~0.80	0.01

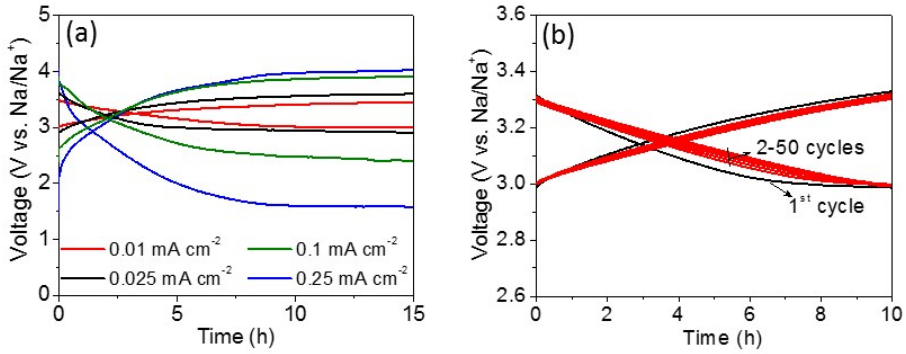

Fig. S12. (a) Charge-discharge curves of porous carbon@carbon paper at different current density (0.01-0.25 mA cm^{-2}) and (b) Cycle performance of porous carbon@carbon paper.

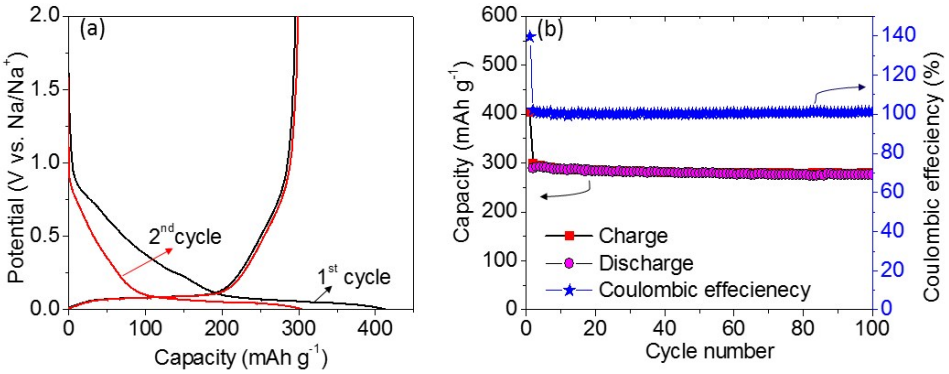

Fig. S13. Electrochemical performance of the 2032 coin-type half-cell (Na|hard carbon). (a) Galvanostatic sodiation/desodiation profiles of the first and second cycles of hard carbon at 20 mA g^{-1} and (b) cycle performance of hard carbon over 100 cycles at 20 mA g^{-1}.

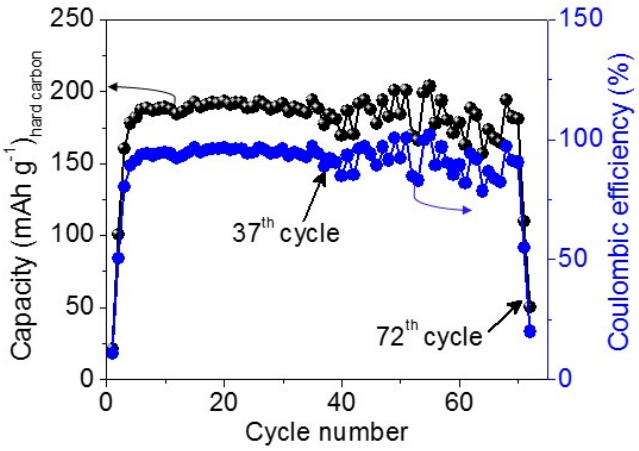

Fig. S14. Cycle performances of full cell based on carbon paper at 0.05 mA cm^{-2}.

References

1 S. M. Hwang, J. Kim, Y. Kim and Y. Kim, *J. Mater. Chem. A*, 2016, **4**, 17946-17951.

2 N. Le Bozec, C. Compère, M. L'Her, A. Laouenan, D. Costa and P. Marcus, *Corros. Sci.*, 2001, **43**, 765–786.

3 J.-K. Kim, F. Mueller, H. Kim, D. Bresser, J.-S. Park, D.-H. Lim, G.-T. Kim, S. Passerini and Y. Kim, *NPG Asia Mater.*, 2014, **6**, e144.

4 H. Kim, J.-S. Park, S. H. Sahgong, S. Park, J.-K. Kim and Y. Kim, *J. Mater. Chem. A*, 2014, **2**, 19584–19588.

5 J.-K. Kim, E. Lee, H. Kim, C. Johnson, J. Cho and Y. Kim, *ChemElectroChem*, 2015, **2**, 328–332.

6 B. Delley, *J. Chem. Phys.*, 1990, **92**, 508.

7 B. Delley, *J. Chem. Phys.*, 2000, **113,** 7756 .

8 J. P. Perdew, K. Burke and M. Ernzerhof, *Phys. Rev. Lett.*, 1996, **77**, 3865–3868.

9 S. GRIMME, *J. Comput. Chem.*, 2010, **31**, 2967–2970.

10 B. Delley, *Mol. Simul.*, 2006, **32**, 117–123.

11 J. Rossmeisl, A. Logadottir and J. K. Nørskov, *Chem. Phys.*, 2005, **319**, 178–184.
12 J. K. Nørskov, J. Rossmeisl, A. Logadottir, L. Lindqvist, J. R. Kitchin, T. Bligaard and H. Jónsson, *J. Phys. Chem. B*, 2004, **108**, 17886–17892.
13 J. Rossmeisl, Z. W. Qu, H. Zhu, G. J. Kroes and J. K. Nørskov, *J. Electroanal. Chem.*, 2007, **607**, 83–89.